Multilayer aberration correction for depth-independent three-dimensional crystal growth in glass by femtosecond laser heating

AUTHOR(S):

Stone, Adam; Jain, Himanshu; Dierolf, Volkmar; Sakakura, Masaaki; Shimotsuma, Yasuhiko; Miura, Kiyotaka; Hirao, Kazuyuki

CITATION:

Stone, Adam ...[et al]. Multilayer aberration correction for depth-independent three-dimensional crystal growth in glass by femtosecond laser heating. Journal of the Optical Society of America B 2013, 30(5): 1234-1240

ISSUE DATE:

2013-05-01

URL:

http://hdl.handle.net/2433/194006

Multilayer aberration correction for depth-independent three-dimensional crystal growth in glass by femtosecond laser heating

Adam Stone,[1] Himanshu Jain,[1,*] Volkmar Dierolf,[2] Masaaki Sakakura,[3] Yasuhiko Shimotsuma,[4] Kiyotaka Miura,[4] and Kazuyuki Hirao[4]

[1]*Department of Materials Science and Engineering, Lehigh University, 5 East Packer Avenue, Bethlehem, Pennsylvania 18015, USA*
[2]*Department of Physics, Lehigh University, 16 Memorial Drive East, Bethlehem, Pennsylvania 18015, USA*
[3]*Innovative Collaboration Center, Kyoto University, Katsura, Nishikyo-ku, Kyoto 615-8510, Japan*
[4]*Department of Material Chemistry, Kyoto University, Katsura, Nishikyo-ku, Kyoto 615-8510, Japan*
**Corresponding author: h.jain@lehigh.edu*

Received January 30, 2013; accepted March 4, 2013;
posted March 22, 2013 (Doc. ID 183856); published April 19, 2013

Focused femtosecond lasers are known for their ability to modify transparent materials well below the surface with 3D selectivity, but spherical aberration causes degraded focal intensity and undesirable absorption conditions as focal depth increases. To eliminate such effects we have implemented an aberration correction procedure that accounts for multiple refracting layers in order to crystallize $LaBGeO_5$ glass inside a temperature-controlled microscope stage via irradiation through a silica glass window. The correction, applied by a spatial light modulator, was effective at removing the focal depth-dependent degradation and achieving consistent heating conditions at different depths, an important consideration for patterning single-crystal architecture in 3D. Additional effects are noted, which produce a range of crystal cross-section shapes and varying degrees of partial crystallization of the melt.

OCIS codes: (220.4000) Microstructure fabrication; (220.4610) Optical fabrication; (320.2250) Femtosecond phenomena.
http://dx.doi.org/10.1364/JOSAB.30.001234

1. INTRODUCTION

High-repetition-rate femtosecond (fs) pulsed lasers can induce local heating and crystallization of nonlinear optic phases deep inside bulk glass, offering a means to introduce second-order nonlinear properties into glassy optics with three-dimensional (3D) space selectivity [1–4]. Modification of a transparent material by a fs laser relies on its high-energy ultrashort pulses and tight focusing to activate nonlinear absorption mechanisms that only occur above some threshold intensity [5,6], ensuring that absorptive losses in the glass outside the high-intensity focus are small regardless of focal depth. Consequently, single-crystal architecture can in principle be laser patterned inside glass in 3D arrangements. However, as emphasized in our recent work [7,8], complications arise in practice. In particular, crystallization behavior in $LaBGeO_5$ glass is strongly influenced by focal depth due to a reshaping of the heat gradient and the resulting laser-induced structural modifications that precede crystal nucleation.

We hypothesized that these focal depth effects were caused by spherical aberration. This is a well-known problem with spherical lenses, which refract rays near the edge of the lens more strongly than rays near the center such that they do not precisely converge to a common focus. Industrial microscope objectives contain compound lenses designed to correct for the spherical aberration of the lenses themselves, and biological microscope objectives include additional compensation for the aberration induced by cover glass. However, spherical aberration is also introduced by the sample itself when focusing below the surface, as the spherical wavefront of the focused beam refracts nonuniformly across the planar interface [9]. The result is a blurring of the focal intensity along the beam axis that worsens as focal depth is increased. In this work, we investigate our hypothesis by characterizing $LaBGeO_5$ crystals grown inside glass of the same composition by fs laser irradiation while using a spatial light modulator (SLM) to correct for spherical aberration.

2. EXPERIMENT

Glass samples were prepared by melt quenching, with a $25La_2O_3 \cdot 25B_2O_3 \cdot 50GeO_2$ target composition corresponding to the stoichiometry of the ferroelectric $LaBGeO_5$ nonlinear optic crystal. High-purity batch materials of La_2O_3, H_3BO_3, and GeO_2 were weighed (accounting for 1.9 wt. % B_2O_3 loss [10]) and mechanically mixed for 5 h before melting at 1250°C for 30 min. The melt was poured and pressed between steel plates preheated at 500°C, then annealed for 2 h at 650°C ($T_G \sim 670$°C). Samples were cut and polished to optical quality on the top and bottom faces.

A schematic of the optical setup is shown in Fig. 1. Irradiations were performed using a regeneratively amplified Ti:sapphire laser oscillator (Coherent Mira 900) with 800 nm wavelength, 250 kHz repetition rate, and 130 fs pulse width. The beam was passed through a digital liquid-crystal-on-silicon SLM (Hamamatsu) before entering the microscope

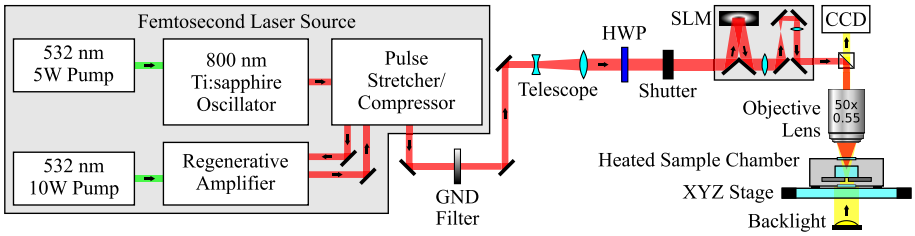

Fig. 1. Schematic of laser optics. Average power is modulated by a graduated neutral-density (GND) filter, the beam diameter is expanded by telescope, a half-wave plate (HWP) rotates the beam polarization for SLM alignment, the SLM imparts customized phase shifts, the objective lens focuses the beam inside the glass sample, and the sample stage allows heating and XYZ mobility.

column. Within the module, the collimated beam was reflected off a 792×600 array of 20 μm pixels, each of which could impart a variable phase shift between 0 and 2π. A 50× magnification objective lens was used (Nikon CFI LU Plan EPI ELWD), with 0.55 numerical aperture (NA), 4 mm focal length, and no aberration compensation for cover glass. The lens was thus assumed to produce an ideal spherical wavefront, and all aberration was assumed to arise from refraction within the focusing geometry. A backlight and CCD camera allowed observation of the focus during irradiation.

Samples were irradiated inside a heated microscope stage in order to suppress cracking of the crystals caused by the stresses associated with phase change and thermal expansion mismatch. The stage was held at 500°C during growth of crystal lines, although irradiations were made at room temperature for initiation of seed crystals and assessment of aberration correction. This heating condition necessitated irradiation of the sample through a 1 mm thick silica glass window, which introduced an additional aberration contribution. Refractive indices of the window and the sample were 1.395 and 1.783, respectively (as calculated by Fresnel reflection using power transmission measurements of the collimated beam). Thus, in terms of optical path length (OPL), the 1 mmwindow effectively resembled an additional 782 μm of focal depth in the bare sample. The 500°C heating did not cause any detectable change in power transmission, so variation of the refractive index with temperature was considered negligible.

A. Aberration Correction

The inverse ray-tracing method used for aberration correction was described by Itoh *et al.* for irradiation of a bare sample [9]. In our case, the silica window of the sample chamber introduced additional aberration, so their derivation was modified to account for an arbitrary number of N refracting layers. The focusing geometry for our $N = 4$ arrangement is illustrated in Fig. 2. Ray *ABCDE* represents the optical path from a point on the lens to an arbitrary focal point. The starting point A can be defined in terms of the unrefracted convergence angle θ, and choosing an intended focal depth d_4 defines the endpoint E. The path *ABCDE* between these two points is then fixed by Fermat's principle, i.e., a ray of light traveling between two points takes the fastest path.

The OPL is the sum of the products of distance traveled and refractive index for each component in the optical path (effectively normalizing for the wavelength shortening that occurs inside materials). The OPL value Φ for path *ABCDE* varies with θ such that without correction, the different angular components of the beam will not generally be in phase at the chosen focal point. By calculating Φ as a function of θ, these relative phase shifts can be quantified and then compensated for by phase shifts at the SLM pixels. This brings all the angular components of the beam into phase at the intended focal point, thereby achieving aberration correction for the chosen focal depth.

Since the refracted angles are all fixed by Snell's law, the value of Φ for a chosen θ can be expressed in terms of only a single angle θ_1 and the refractive index n_i and thickness d_i of each layer i in the optical path. Simplification by trigonometric identity yields

$$\begin{aligned}\Phi(\theta) &= n_1|AB| + n_2|BC| + n_3|CD| + n_4|DE| \\ &= \sum_{i=1}^{N} \frac{n_i d_i}{\cos\,\theta_i} = \sum_{i=1}^{N} \frac{n_i^2 d_i}{\sqrt{n_i^2 - n_1^2 \sin^2\theta_1}}.\end{aligned} \tag{1}$$

The phase shifts introduced by the SLM have a lens-like effect, and θ_1 represents the new incident angle that must result after aberration correction in order for the ray to reach point E. Its value is initially unknown, but the relationship between θ and θ_1 can be obtained geometrically from Fig. 2. Another application of Snell's law and simplification by trigonometric identity yields

$$\sin(\theta) = \frac{n_1\,\sin\,\theta_1}{f} \sum_{i=1}^{N} \frac{d_i}{\sqrt{n_i^2 - n_1^2 \sin^2\theta_1}}. \tag{2}$$

A problem remains that the value of d_1 changes with θ due to the curvature of the lens, as is clear from Fig. 2. To account for this, d_1 can be expressed in terms of θ and the other layer thicknesses (d_i for $i > 1$) according to

$$d_1 = f\,\cos\,\theta + d_N - d_f - \sum_{i=2}^{N} d_i. \tag{3}$$

Here d_f is the depth of the intrinsic focal point of the lens in the absence of refraction (Fig. 2). This substitution can be employed in both Eqs. (1) and (2) to remove the d_1 terms.

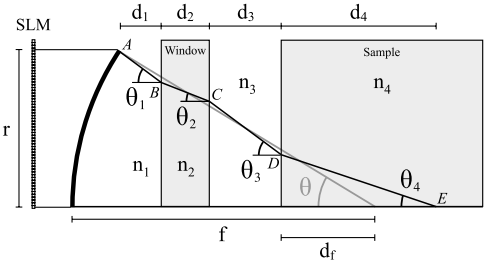

Fig. 2. Focusing geometry used in aberration correction (see Section 2.A for a discussion of terms).

Applying additional trigonometric identities to collect the θ terms, Eq. (2) becomes

$$\sin(\theta-\theta_1)=\frac{n_1\sin\theta_1}{f}\left(d_N-d_f+\sum_{i=2}^{N}\frac{d_i\cos\theta_1}{\sqrt{n_i^2-n_1^2\sin^2\theta_1}}-d_i\right). \tag{4}$$

Equations (1) and (4) describe the general case for aberration correction in a multilayer system, such as focusing through a window into a sample chamber with a non-air atmosphere. In our case an air atmosphere was used, and the temperature dependence of n_{air} was considered negligible, such that $n_3=n_1=1$. The d_3 terms in Eqs. (1) and (4) then cancel out, and only the thicknesses of the window $d_2=d_w$ and the intended focal depth in the sample $d_4=d$ must be known, along with the refractive indices of the window $n_2=n_w$ and sample $n_4=n_s$. For this special case, Eq. (1) becomes

$$\Phi(\theta)=\frac{f\cos\theta-d_f-d_w}{\cos\theta_1}+\frac{n_w^2 d_w}{\sqrt{n_w^2-\sin^2\theta_1}}+\frac{n_s^2 d_s}{\sqrt{n_s^2-\sin^2\theta_1}}, \tag{5}$$

and Eq. (4) becomes

$$\sin(\theta-\theta_1)=\frac{\sin(2\theta_1)}{2f}\times\left(\frac{d_w}{\sqrt{n_w^2-\sin^2\theta_1}}+\frac{d}{\sqrt{n_s^2-\sin^2\theta_1}}-\frac{d_f+d_w}{\cos\theta_1}\right). \tag{6}$$

Since Eqs. (4) and (6) cannot be rearranged to solve for $\theta_1(\theta)$, Newton's method was used to numerically approximate the value of θ_1 for each θ of interest. The discrete θ values were obtained for each pixel on the SLM screen according to $r=mf\sin\theta$, where r is the radial distance of the pixel from the center of the grid and m is the internal magnification of the SLM module (in our case $m=2$). Substituting the obtained θ and θ_1 values into Eq. (5), a phase shift was obtained for each pixel equal to the OPL difference with respect to the center of the beam, $\Delta\Phi(\theta)=\Phi(\theta)-\Phi(0)$, mod 2π. In principle, pixels outside the maximum range of the lens aperture, $\theta_{\max}=\sin^{-1}(\text{NA})$, should not affect the focal intensity. Nevertheless, these were assigned random phase values for destructive interference as a precaution to minimize any unintended influence.

As a consequence of eliminating the d_1 terms, obtaining $\Delta\Phi(\theta)$ required specifying a value for d_f, the position of the intrinsic focal point of the lens in the absence of refraction. This could be chosen arbitrarily, but a choice may be considered optimal that minimizes the peak-to-valley value of the phase pattern (i.e., the maximum phase shift between angular components of the beam). In general this occurs when $\Delta\Phi(\theta_{\max})=0$. Thus, before calculating each correction pattern, the optimum value of d_f was found by iteratively refining an initial guess until $\Delta\Phi(\theta_{\max})\sim 0$ was obtained. The aberration correction pattern was then calculated and added to a baseline pattern provided by the SLM manufacturer (a correction for small distortions of the SLM surface) to yield the final pattern.

B. Irradiation

Since the correction patterns have circular symmetry, alignment of the SLM screen was necessary to ensure that the pattern center coincided with the center of the beam. This alignment was evaluated by removing the sample chamber and placing a paper well below the focal point of the beam in order to view a projected image of the phase map. The aperture at the SLM input was then varied to ensure that the pattern remained centered as the aperture was opened and closed. The projected image also revealed whether the pattern was scaled correctly, in which case the edge of the pattern at $\theta_{\max}$ occurred just at the edge of the projected circle with the aperture fully open.

For each focal depth, the sample must be positioned to place the intrinsic focal point of the lens at the same d_f value used in calculating the phase map. For a bare sample this should be as simple as focusing on the surface, then applying a displacement z along the vertical axis equal to the calculated value of d_f. Including the window complicates the situation: focusing the image on the sample surface through the window results in $d_f<0$ (above the surface) due to refraction by the window. In other words, a shift Δd is introduced between d_f and the required stage displacement z. Focusing at an arbitrary depth thus involved a two-step process. (1) The beam was first focused on the surface at very low power with an aberration correction pattern calculated for $d=0$. The negative value obtained for optimized d_f when $d=0$ was taken as the shift Δd. (2) The correction pattern was then changed to correspond to the intended focal depth, and the optimized d_f for this new pattern was used to move the stage vertically into the correct position according to $z=d_f-\Delta d$. All references to "focal depth" herein will refer to the real distance of the focus below the sample surface (rather than the stage displacement), which in the uncorrected cases was approximately $2z$.

Producing a seed crystal required particular aberration conditions to achieve heterogeneous nucleation, as discussed in [8]. Seed crystals were established at room temperature (but inside the heating chamber, irradiated through the window) and with no aberration correction applied. The range of focal depths conducive to nucleation could be shifted and expanded by increasing the laser power, suggesting that focal depth and laser power are the main process parameters to be optimized for crystal nucleation. An unidentified crystalline phase typically appeared first, but $LaBGeO_5$ eventually appeared if irradiation was continued (indicated by a sudden increase in second harmonic intensity) [7]. With a high power of 700–800 mW, seed crystals could be initiated in the 500–1000 μm range within several minutes of irradiation and then grown upward to other depths.

The $LaBGeO_5$ seeds were grown into crystal lines by moving the sample stage horizontally at controlled speeds while aberration correction was applied for focal depths of 100, 500, and 1000 μm. During growth, the sample was heated to 500°C to relieve stress and suppress cracking. This heating was found to introduce instability in the focal position, which was attributed to refractive effects of hot air convection in the beam path. Placing a small fan above the window minimized this instability. Crystal lines were grown in parallel from a single orthogonal line at each depth, and samples were annealed at 650°C for 2 h to relieve residual stress before cutting and polishing to reveal line cross sections. The lines were characterized by optical microscopy, LC-PolScope imaging, and field

emission scanning electron microscopy (SEM) (Hitachi 4300) with electron backscatter diffraction (EBSD).

3. RESULTS AND DISCUSSION

A. Aberration Correction

The effectiveness of the aberration correction procedure was assessed by comparing the shape and size of heat modifications produced at different focal depths with and without the aberration correction pattern applied (uncorrected cases used only the baseline distortion-correction pattern). Heat modification here refers to the refractive-index-modified glass volume that appears prior to crystallization. The boundary of this region occurs near the glass transition temperature (T_G) [11], so its shape and size reflect the influence of aberration on the distribution of laser intensity near the focal region and the resulting heat flux.

Figure 3 shows heat modifications from uncorrected and corrected irradiations for two focal depths, with and without the presence of the window, and the corresponding aberration correction patterns. The worsening effect of aberration on the irradiation profile with increasing depth is obvious. In general, aberration-corrected irradiation profiles resemble uncorrected irradiation profiles only near the surface, where aberration is small. Although elongation at large focal depths is significantly reduced by the correction procedure, the shape remains elliptical, with a thin tail remaining at the bottom. In any case, the correction procedure does effectively normalize the shape and size of the modifications for a given laser power, allowing the use of much lower power at high focal depth and a consistent power across all focal depths with minimal change in size and shape of the heat-modified region.

B. Crystal Growth

Figure 4 shows examples of crystal lines grown with and without aberration correction at 500 and 1000 μm focal depths, irradiated through the heating stage window with a 500°C sample temperature. The upper part of each frame shows an LC-PolScope image of various lines as viewed from above, which visualizes the birefringence of the crystals; the lower part shows the cross section in a standard optical micrograph. In the LC-PolScope images, each crystal effectively acts like a waveplate on circularly polarized light passing through it, retarding the polarization component parallel to the "slow axis" of the crystal with respect to the orthogonal "fast axis" in the plane of the image. The brightness in these images indicates the measured retardance, and the color indicates the orientation of either the slow or the fast axis of the crystal. Note that while the total retardance increases with the thickness of the crystal, the measured retardance is cyclic, as each full 2π delay results in a return to the initial polarization condition. This creates ambiguity in determining which of the polarization axes is slowed with respect to the other, so a single crystal may still exhibit fringes of alternating colors corresponding to varying thickness. The colored fringes in Fig. 4 thus provide a measure of the thickness of the crystal as viewed from above (effectively, the cross-section shape), and the uniformity of the crystal cross section down the length of the line can be quickly gauged based on the variation of these features.

Figures 4(a) and 4(b) show aberration-corrected lines written at 500 and 1000 μm depths, respectively, with 300 mW average power and scan speeds near 44 μm/s, the limit at which the crystal could most consistently follow the laser. Each cross section exhibits an elliptical laser-modified region that contains one or more crystals (generally brighter, more sharply defined features indicated by white arrows) and

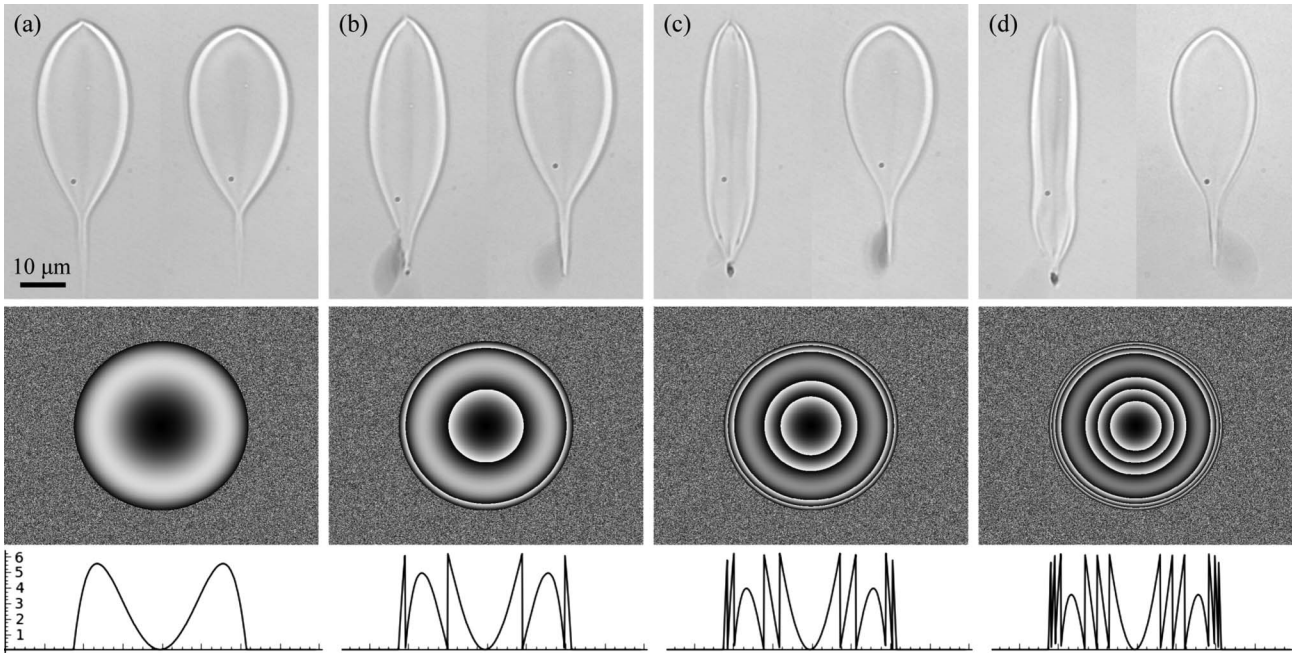

Fig. 3. Effect of aberration correction, in order of increasing aberration from (a) to (d). Laser heat-modification profiles (laser incident vertically from above) were produced at room temperature by 30 s, 300 mW irradiation focused in the *bare sample* at (a) 0.5 mm and (b) 1 mm below the surface, and focused *through the silica glass window* at (c) 0.5 mm and (d) 1 mm below the sample surface. Each frame compares uncorrected and aberration-corrected irradiations (left and right, respectively), with the corresponding aberration correction pattern and its phase profile (varying from 0 to 2π) shown below.

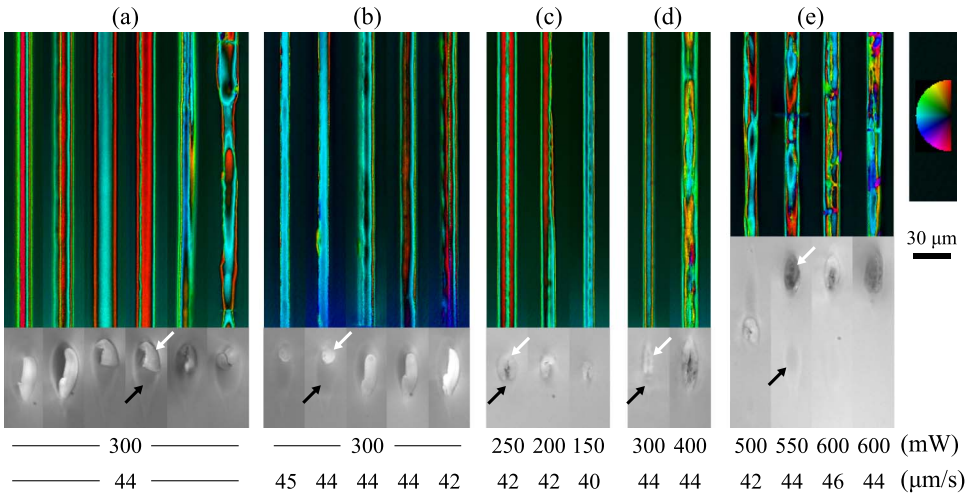

Fig. 4. LC-PolScope and transmission optical micrographs of crystal lines and their cross sections, respectively, written under various conditions. Lines are oriented with the cut surface near the bottom of the image. Average laser power and scanning speed of the focus are indicated below each cross section, and the color wheel indicates the orientations of the fast or slow axes in the LC-PolScope images. Groups (a), (c), and (d) were written at a 500 μm depth, and (b) and (e) at a 1000 μm depth. Groups (a), (b), and (c) were aberration-corrected; (d) and (e) were not. White arrows indicate crystals, and black arrows indicate laser-modified glass.

residual refractive-index-modified glass (generally darker, lower-contrast features indicated by black arrows). The effectiveness of aberration correction is seen in the overall modification shape and size, which is approximately constant between all the lines in Figs. 4(a) and 4(b). This indicates that the focal intensity and heating conditions were approximately the same for all lines despite the difference in focal depth. Nevertheless, the particular shape and position of crystals within the modified regions and the amount of residual glass are seen to vary from line to line, even among the lines where conditions were held constant (within experimental error). Based on the LC-PolScope images, the lines also exhibit varying uniformity down their length [compare, for example, the first two lines in Fig. 4(a) with the last two lines]. It thus appears that a particular heating condition can support multiple potential morphologies, some more stable than others, and inconsistency in crystalline features may occur even when aberration effects are minimized. We expect that the particular shape adopted by each crystal down the length of the lines may depend strongly (and somewhat unpredictably) on the very early growth behavior of each new line as it is initiated from the seed. The stability of these different growth morphologies to small fluctuations in heating conditions may then determine whether a particular cross-section shape can be grown uniformly over long distances.

Figure 4(c) shows corrected irradiations with decreasing laser power (which also reduced the limiting speed). The crystals exhibit preferential growth around the periphery of the heat modification in all observed cases, but lower average powers appear more likely to produce bilateral horseshoe-shaped cross sections, while higher average powers more often show unilateral growth limited to one side or the top of the heat modification. The 200 mW case in Fig. 4(c) shows a transition between the two cases, where the left side (red) becomes dominant and the thinner right side (blue) terminates as the line progresses from the bottom to the top of the image.

The tendency for peripheral crystal growth is likely caused by the heat source at the center reaching higher than optimal temperature for crystallization, potentially exceeding the melting point of the crystal [11]. The variation of crystal profile among partially crystallized outcomes can be understood in terms of the temperature and orientation dependence of the crystal growth rate and its relation to the scanning speed. The $LaBGeO_5$ crystal consistently aligns its fastest-growing axis with the direction of focal point scanning, with the fastest growth occurring in the scanning direction and localized at the particular positions within the heat modification where temperature is optimum. Growth orthogonal to the scanning direction and at suboptimal temperatures may be much slower due to the inherent anisotropy of the crystal and the range of temperature conditions across the heat modification. As such, the crystal may keep up with the focal point in the writing direction but fail to fully expand laterally (particularly at scanning speeds near the crystal growth rate limit), yielding many potential cross-section geometries. Some shapes appear to be more stable than others and recur in multiple lines.

Figures 4(d) and 4(e) compare uncorrected lines written at 500 and 1000 μm depths, respectively. Uncorrected lines are generally very nonuniform at these depths, with occasional exceptions like the 300 μm/s case in Fig. 4(d). The heat modifications are more elongated and exhibit horseshoe-shaped cross sections in all observed lines. Unlike the corrected cases, substantial variation is seen between the two focal depths, due to the increasing aberration, and higher average power is needed to obtain comparable crystal width as aberration increases. For most lines in the higher-aberration 1000 μm case, two distinct heat-modified regions remain after annealing. This reflects an aberration-induced division of the optical intensity into two regions, which become increasingly separated as focal depth is increased.

C. Crystal Orientation

Figure 5 shows SEM crystal orientation data from the polished cross section of the first line in Fig. 4(a), collected in variable-pressure mode at 15 Pa and 20 kV with no conductive coating. In such conditions, dielectric crystals can exhibit charge contrast that reveals additional details about the defect state of

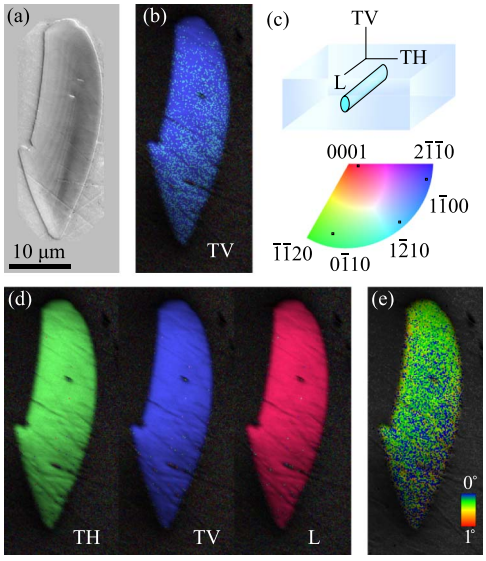

Fig. 5. SEM crystal orientation data from the cross section of the first line in Fig. 4(a). (a) The ESED image reveals light and dark regions within the crystal, but these do not correspond to any features in the crystal orientation IPF maps. (b) An as-collected map for the TV direction shows a primary orientation near $[2\bar{1}\,\bar{1}\,0]$ containing scattered pixels of a secondary orientation near $[1\bar{2}10]$, which can be attributed to pseudosymmetry artifacts. (c) The color correspondence and reference geometry. (d) Pseudosymmetry-corrected IPF maps for three orthogonal reference directions (TV, TH, and L) unambiguously reveal a single crystal with longitudinal orientation near [0001]. (e) The GAOD map shows only random noise, with relative misorientations of less than 1° and no evidence of distinct low-angle grain boundaries.

the crystal absent in other imaging modes [12]. In this case, the environmental secondary electron detector (ESED) image in Fig. 5(a) reveals distinct features that suggest that the density of charge-trapping sites varies across the crystal due to differences in impurity, dislocation, vacancy, or constituent concentrations [13,14].

Channeling contrast between differently oriented crystal grains could also exhibit such features, but inverse pole figure (IPF) orientation maps reveal no correspondence between these features and the crystal orientation. Figure 5(b) shows an as-collected map of the crystal orientation along the transverse vertical (TV) direction with respect to the line (vertical in the plane of the line cross section). In such IPF maps, the colors indicate the orientation of the crystal lattice along a reference direction; the color correspondence and the reference geometry for this case are illustrated in Fig. 5(c). A gray-scale image quality filter was also applied to mask those pixels where a diffraction pattern could not be obtained (e.g., glass, cracks, grain boundaries, deep scratches, surface debris). Pixels of a consistent orientation near $[1\bar{2}10]$ appear dispersed throughout a primary orientation near $[2\bar{1}\,\bar{1}\,0]$, but their randomly scattered distribution suggests that these are pseudosymmetry artifacts rather than real features representing distinct grains. Indeed, they could be removed by applying a single 180° pseudosymmetry correction about the $[11\bar{2}0]$ axis.

Figure 5(d) shows pseudosymmetry-corrected orientation maps for the transverse horizontal (TH) and longitudinal (L) directions (horizontal in the plane of the cross section, and normal to the plane of the cross section, respectively) in addition to the TV direction. Comparing three orthogonal directions in this way defines the orientation unambiguously and accounts for possible rotary misorientations about the reference axis of any individual IPF map. Consistent with our earlier results [7,8,15], the line appears to be a *single crystal* with longitudinal orientation close to [0001] (c-axis oriented). This is supported by the grain average orientation deviation (GAOD) map [Fig. 5(e)], which highlights low-angle misorientations with much higher angular resolution than the IPF maps and here shows no systematic misorientations, with nearly all pixels exhibiting relative misorientations of less than 1°. The presence of light and dark regions in the ESED image thus cannot be explained by polycrystallinity and must reflect some intragranular microstructural variation.

4. CONCLUSIONS

Previous work [7,8] showed varying crystallization behavior and formation of inconsistent single-crystal architecture by fs laser irradiation in glass, which depended on the depth of focus below the surface. To solve this problem, an aberration-correction procedure was derived for the case of multiple refracting layers, based on the inverse ray-tracing method introduced by Itoh *et al.* [9]. This enabled aberration correction during irradiation and crystallization of heated glass samples behind a heating stage window. The correction, implemented with an SLM, was successful at producing heat modifications with consistent shape and size for a given laser power, independent of focal depth. A detailed analysis of the orientation of a laser-written line by EBSD confirms its single-crystal nature, while growing very closely along the [1000] direction. Within the crystal there are indications of distinct regions differing in density of charge-trapping sites. The origin of these features is currently under investigation.

Thus, the present results have validated our hypothesis that depth-dependent variation of the temperature profile and consequent crystallization occur primarily due to aberration effects, which can be corrected following the procedure proposed here. As such, aberration correction is a necessary step for achieving the consistent heating conditions needed for patterning 3D crystal arrangements inside glass over significant focal depth ranges. However, aberration correction alone may not guarantee simple, symmetric crystal cross sections. For example, although the correction removes the excess elongation seen in uncorrected heat modifications at large focal depths, it does not yield a fully circular cross section, and significant inherent ellipticity remains. More advanced beam-shaping methods and other optimizations in addition to aberration correction may ultimately be required for growth of consistently uniform crystals with a well-controlled shape.

ACKNOWLEDGMENTS

We are grateful to the National Science Foundation for initiating and supporting our international collaboration through the International Materials Institute for New Functionality in Glass (IMI-NFG) (DMR-0844014 and DMR-0906763).

REFERENCES

1. K. Miura, J. Qiu, T. Mitsuyu, and K. Hirao, "Space-selective growth of frequency-conversion crystals in glasses with ultrashort infrared laser pulses," Opt. Lett. **25**, 408–410 (2000).
2. Y. Yonesaki, K. Miura, R. Araki, K. Fujita, and K. Hirao, "Space-selective precipitation of non-linear optical crystals inside

silicate glasses using near-infrared femtosecond laser," J. Non-Cryst. Solids **351**, 885–892 (2005).
3. Y. Dai, B. Zhu, J. Qiu, H. Ma, B. Lu, S. Cao, and B. Yu, "Direct writing three-dimensional $Ba_2TiSi_2O_8$ crystalline pattern in glass with ultrashort pulse laser," Appl. Phys. Lett. **90**, 181109 (2007).
4. B. Zhu, Y. Dai, H. Ma, S. Zhang, G. Lin, and J. Qiu, "Femtosecond laser induced space-selective precipitation of nonlinear optical crystals in rare-earth-doped glasses," Opt. Express **15**, 6069–6074 (2007).
5. B. Rethfeld, O. Brenk, N. Medvedev, H. Krutsch, and D. H. H. Hoffmann, "Interaction of dielectrics with femtosecond laser pulses: application of kinetic approach and multiple rate equation," Appl. Phys. A **101**, 19–25 (2010).
6. C. L. Arnold, A. Heisterkamp, W. Ertmer, and H. Lubatschowski, "Computational model for nonlinear plasma formation in high NA micromachining of transparent materials and biological cells," Opt. Express **15**, 10303–10317 (2007).
7. A. Stone, M. Sakakura, Y. Shimotsuma, G. Stone, P. Gupta, K. Miura, K. Hirao, V. Dierolf, and H. Jain, "Formation of ferroelectric single-crystal architectures in LaBGeO5 glass by femtosecond vs. continuous-wave lasers," J. Non-Cryst. Solids **356**, 3059–3065 (2010).
8. A. Stone, M. Sakakura, Y. Shimotsuma, G. Stone, P. Gupta, K. Miura, K. Hirao, V. Dierolf, and H. Jain, "Unexpected influence of focal depth on nucleation during femtosecond laser crystallization of glass," Opt. Mater. Express **1**, 990–994 (2011).
9. H. Itoh, N. Matsumoto, and T. Inoue, "Spherical aberration correction suitable for a wavefront controller," Opt. Express **17**, 14367–14373 (2009).
10. V. N. Sigaev, S. Y. Stefanovich, P. D. Sarkisov, and E. V. Lopatina, "Lanthanum borogermanate glasses and crystallization of stillwellite $LaBGeO_5$: I. Specific features of synthesis and physicochemical properties of glasses," Glass Phys. Chem. **20**, 392–397 (1994).
11. M. Sakakura, M. Shimizu, Y. Shimotsuma, K. Miura, and K. Hirao, "Temperature distribution and modification mechanism inside glass with heat accumulation during 260 kHz irradiation of femtosecond laser pulses," Appl. Phys. Lett. **93**, 231112 (2008).
12. B. L. Thiel and M. Toth, "Secondary electron contrast in low-vacuum/environmental scanning electron microscopy of dielectrics," J. Appl. Phys **97**, 051101 (2005).
13. K. Robertson, R. Gauvin, and J. Finch, "Application of charge contrast imaging in mineral characterization," Minerals Eng. **18**, 343–352 (2005).
14. G. R. Watt, B. J. Griffin, and P. D. Kinny, "Charge contrast imaging of geological materials in the environmental scanning electron microscope," Am. Mineralogist **85**, 1784–1794 (2000).
15. A. Stone, M. Sakakura, Y. Shimotsuma, G. Stone, P. Gupta, K. Miura, K. Hirao, V. Dierolf, and H. Jain, "Directionally controlled 3D ferroelectric single crystal growth in LaBGeO5 glass by femtosecond laser irradiation," Opt. Express **17**, 23284–23289 (2009).